

Multi-oriented moiré superstructures of graphene on Ir(111): experimental observations and theoretical models

Lei Meng, Rongting Wu, Lizhi Zhang, Linfei Li, Shixuan Du, Yeliang Wang and H-J Gao

Institute of Physics, Chinese Academy of Sciences, Beijing 100190, People's Republic of China

E-mail: sxdu@iphy.ac.cn and ylwang@iphy.ac.cn

Received 11 April 2012, in final form 15 May 2012

Published 20 July 2012

Online at stacks.iop.org/JPhysCM/24/314214

Abstract

Six types of moiré superstructures of graphene on Ir(111) with different orientations (labeled as R0, R14, R19, R23, R26 and R30) are investigated by low-energy electron diffraction, scanning tunneling microscopy and first-principles calculations. The moiré superstructure of R0 graphene has remarkable diffraction spots and deeper corrugation than that of the other superstructures. A high-order commensurate (HOC) method is applied to produce a list of all possible graphene moiré superstructures on Ir(111). Several useful structural data including the precise matrices of the moiré patterns are revealed. Density functional theory based first-principles calculations that include van der Waals interactions reveal the differences of the geometric environment and electronic structures of carbon atoms with respect to the underlying Ir(111) lattices for all the observed moiré patterns. The further calculations of electronic properties at the graphene–Ir interfaces show that the electron transfers for all superstructures are small and of the same order of magnitude, which demonstrates a weak interaction between graphene and the Ir(111) substrate, leading to the coexistence of multi-oriented moiré superstructures.

(Some figures may appear in colour only in the online journal)

1. Introduction

As a new type of two-dimensional material with a single layer of carbon packed in a honeycomb lattice, graphene holds enormous application potential in advancing the development of microelectronics. Since it was initially exfoliated from graphite in 2004 [1], it has demonstrated unique properties in various of aspects, such as electronics, magnetism and optics [2–6]. The pursuit of either new physical discoveries about graphene materials or their potential applications demands high-quality samples of single-layer graphene. Graphene prepared by exfoliation shows a high quality suitable for fundamental research, but its dimensions, always in micrometers, are obviously not big enough for the integration of devices. The demand for industrial-scale sizes of graphene aroused considerable interest in its fabrication in scientific and technological fields [7–10], and thus the

preparation of high-quality graphene becomes a formidable task.

One established method to make large-scale graphene is epitaxial growth on a transition metal substrate, which favors the formation of graphene by serving as a catalyst or template. Recently, high-quality graphene has been achieved in a controlled way by hydrocarbon decomposition on polycrystalline copper foils or single-crystalline surfaces like Ni(111) [11], Ru(0001) [12–16], Ir(111) [17–22], Cu(111) [23, 24], and Pt(111) [25, 26]. In many cases, graphene samples made by epitaxial growth can provide products of macroscopic scale [16].

Two features are noteworthy in these graphene/metal systems. First, graphene and these metal substrates have slightly different lattice parameters but the same hexagonal symmetry. Second, graphene and the metal substrate interact, strongly or weakly. Owing to these two features, graphene

(Gr) may be strained or be rotated with respect to the substrate structure, in order to minimize the total energy of the system. Normally, such rotations between two different lattices lead to the formation of moiré superstructures. If the substrate interaction with graphene is relatively strong, as in Gr/Ru(0001) [16], a uniform moiré pattern is likely. Otherwise, several types of moiré patterns coexist, as in Gr/Pt(111) [26] and Gr/Ir(111) [27, 28]. Besides the effect of the lattice constant, the emergence of moiré patterns of the graphene adlayer are sometimes influenced by the growth parameters and the quality of the substrate itself [26, 29].

As moiré superstructures generally appear along with graphene, people try to utilize the advantages of these well-ordered two-dimensional superstructures and find many exciting phenomena. For example, the size of mono-dispersed platinum nano-clusters can be well controlled by using moiré superstructures of graphene on Ru(0001) [30]. Also, self-assembled phthalocyanine molecules can form regular Kagome lattices on Gr/Ru(0001) that duplicate the lattice of the moiré superstructures [31]. On a Gr/Ir(111) surface, selective hydrogen adsorption on the moiré superstructure can open a gap in graphene [32]. Very recent findings show that differently oriented moiré superstructures hold different electronic properties [33, 34]. Even more interesting, a corrugated graphene adlayer on metal behaves as a quantum well with localized electronic confinement in the moiré superlattice [35–39]. As seen, the moiré pattern of graphene is a very promising template for nanostructures with wonderful properties. Thus, more in-depth understanding of these moiré superstructures of graphene is needed. Actually, studies of epitaxial rotation of the moiré superstructure date back to 1977 [40]. After that, an array of researchers began to investigate the relationship of moiré superstructures with the rotation by various theoretical methods [41–44]. Recently, a strain-driven model for moiré superstructures of graphene on transition metals has been proposed [45]. This model claims to predict all possible moiré superstructures of graphene on several metal substrates. But obtaining the precise configuration such as the matrix of moiré superstructures with respect to the substrate lattice still requires effort.

Since previous reports have mainly focused on the growth and structures of graphene on Ir(111), here, we concentrate mainly on the interface properties of different moiré superstructures of graphene on Ir(111). Growth temperature has a dramatic influence on the quality of graphene as we previously reported specifically for the case of different rotational graphene domains on the Pt(111) surface [26]. For the present study, we thus change the growth temperature to induce different orientations of graphene on Ir(111). The as-prepared samples are then characterized by low-energy electron diffraction (LEED) and scanning tunneling microscopy (STM). We further use an improved high-ordered commensurate (HOC) [46] formula to gain a list of possible graphene moiré patterns on Ir(111) as well as the corresponding geometric parameters including the precise matrices. Moreover, in order to understand the moiré superstructures more precisely and the interface properties, we have done density functional theory (DFT)

based first-principles calculations. Combining experimental observations with calculation results, we reveal the geometric and electric properties at the graphene–Ir interfaces of six moiré patterns in detail. The electron transfer at the interface shows that the interaction between the graphene layer and the substrate is weak and the graphene layer is slightly p doped.

2. Methods

The experiment was performed in an ultra-high vacuum (UHV) system with a base pressure about 2×10^{-10} mbar. The Ir(111) single crystal (Mateck) was cleaned by several cycles of sputtering followed by annealing in O₂ atmosphere ($\sim 1 \times 10^{-6}$ mbar) to remove the carbon contaminant. After this treatment, a distinct Ir(1 × 1) LEED pattern and clean terraces in STM image are observed. This clean Ir(111) substrate is heated to 1120 K and exposed to ethylene (partial pressure 1×10^{-6} mbar) for 90 s, and then is further heated to a much higher temperature in the range of 1120–1500 K. Graphene is then found on the sample. LEED and STM are employed to investigate the geometric properties of the as-prepared sample.

Our theoretical calculations are based on DFT with the plane-wave based program, as implemented in the Vienna *ab initio* simulation package (VASP) [47, 48]. The projector augmented wave (PAW) potentials are used to describe the core electrons and the generalized gradient approximation of Perdew, Burke, and Ernzerhof (PBE) for exchange and correlation [49]. We use Grimme’s empirical correction scheme to take into account the van der Waals (vdW) interaction [50], and the standard values of the calculation parameters are used in these DFT + D/PBE calculations [51] (the coefficient C_6 for iridium is the same as Au [52]). The periodic slab models include three layers of iridium, one layer of graphene, and a vacuum layer of 15 Å. All the atoms are fully relaxed except for the bottom two substrate layers until the net force on every atom is less than 0.01 eV \AA^{-1} . In our calculation, the energy cutoff of the plane-wave basis sets is 400 eV, and different K-points sampling is chosen for different models, where $9 \times 9 \times 1$ for R30 graphene, $2 \times 2 \times 1$ for R26 graphene, $3 \times 3 \times 1$ for R23 graphene, $5 \times 5 \times 1$ for R19 graphene, $3 \times 3 \times 1$ for R14 graphene, and a single Γ point for R0 graphene are employed for Brillouin zone matrix integrations.

3. Results and discussion

3.1. Multi-oriented moiré superstructures of graphene at Ir(111)

We found six orientations of graphene on the Ir(111) surface by LEED. These orientations are consistent with previously reported works [17, 27, 28]. In their works, they independently detected several patterns with these orientations by LEED and low-energy electron microscopy (LEEM) and described these patterns as R0, R14, R18.5, R22, R26, and R30. The R0 and R30 graphene was also revealed by STM. In our experiment, we found all the

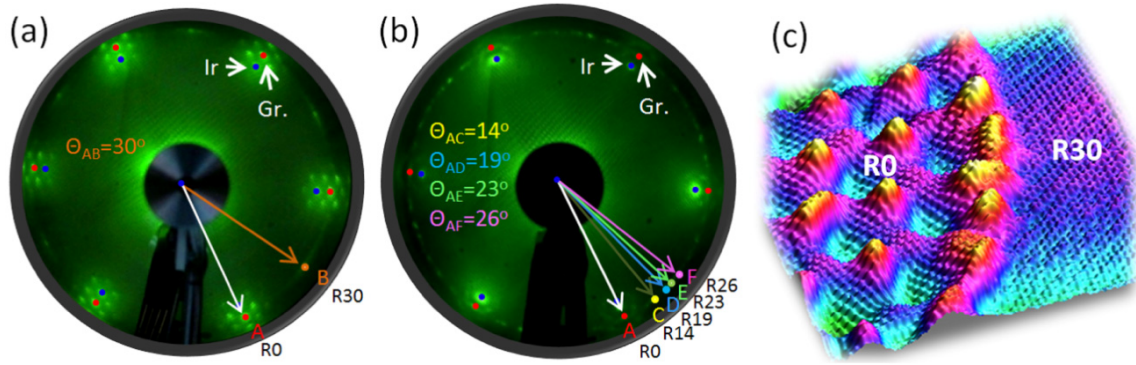


Figure 1. LEED patterns and STM images of differently oriented graphene on Ir(111). In (a) and (b), the inner six diffraction spots (marked in blue) are from Ir substrate, and the outer six spots (marked in red) surrounded by satellite dots are from R0 graphene, denoted by the long white arrow. R30 graphene is denoted by a brown arrow, illustrating its relative rotation. (b) R14, R19, R23 and R26 graphene are denoted by yellow, light blue, green, and pink arrows respectively. (c) Atomic resolution STM image (12 nm × 12 nm) of R0 and R30 graphene domains in three-dimensional view. R0 graphene has deeper corrugation than R30 graphene. The beam energy is 76 eV and 68 eV in (a) and (b), respectively.

six orientations of graphene on Ir(111) substrate. Figure 1 displays the LEED patterns of graphene on Ir(111) obtained at different growth temperatures. In figure 1(a), the inner six spots (highlighted as blue) originate from the six-fold symmetry of the Ir(111) substrate, and the outer six spots (in red) surrounded by satellite points are ascribed to the R0 graphene. The close-packed directions of Ir[110] and R0 graphene [1120] are parallel to each other. Besides, there is another set of outer spots rotated by 30°, which result from the R30 graphene domain. This set of spots means the rotation angle between the directions of Ir[110] and R30 graphene [1120] is 30°. In figure 1(b), except for the R0 graphene, arc-shaped spots emerge. Four types of oriented (R14, R19, R23, R26) graphene can be distinguished from the arc-shaped spots, as denoted by yellow, light blue, green, and pink arrows, respectively.

Multiple orientations of graphene are prone to emerge on the same substrate, which may result from the mismatch and weak interaction between graphene lattice and the underlying Ir(111) lattice. The mismatch normally causes corrugation in an adlayer or even moiré superstructures with different periodicities and orientations. In order to see possible moiré superstructures as well as their corrugations in real space, we use STM to investigate the geometric properties of the graphene adlayer. Figure 1(c) represents a typical STM image in three-dimensional view. It reveals the difference of topography between the R0 and R30 graphene domains. The periodic corrugation of R0 graphene is obviously much more extreme than that of R30 graphene. The corrugation in between the grain boundaries is probably due to enhanced electronic density states caused by the atomic defects between two rotated domains, which is similar to previous findings in the graphite system [53, 54].

Figure 2 shows more of the structural features of four rotated graphene domains on Ir(111), described as R0, R14, R19, and R30, including their STM images in atomic resolution and the corresponding fast Fourier transform (FFT) patterns. Here, the atomically resolved STM image of the R30 domain (figure 2(d)) shows a moiré pattern with a

periodicity of 0.5 nm, however, in this domain we did not observe the second-order moiré superstructure with a larger periodicity as reported by McCarty’s group [27]. Such a difference in STM images may be due to the different tip condition and the scanning parameters. The rhombus in each STM images denotes one moiré unit cell of each domain, corresponding to graphene (10 × 10), (4 × 4), (3 × 3), and (2 × 2) lattice, respectively. In figure 2, the close-packed directions of graphene [1120] (marked by dashed-line arrows) and the moiré superlattices (marked by solid-line arrows) of differently rotated domains are pointed out. From the atomically resolved STM image of R0 graphene, we can easily get the direction of Ir[110] by a combination of the LEED patterns in figure 1, in which the directions of Ir[110] and graphene [1120] are parallel in R0 graphene. Also, we can get the relative rotation angle between each graphene domain and Ir substrate through the FFT image, using the following formula $\vec{k}_1 - \vec{k}_2 = \vec{k}_{\text{moiré}}$. As shown in figures 2(e)–(f), the vectors of the four moiré patterns ($\vec{k}_{\text{moiré}}$) and the graphene lattices (\vec{k}_{Gr}) are indicated by yellow and white dashed lines respectively. Thus, the direction of Ir [110] (\vec{k}_{Ir}) can easily be derived, so can the rotation angles, which are 0°, 14°, 19°, and 30° for the four domains.

3.2. Unveiling the moiré superstructures by HOC models

Recently, a strain-driven model was proposed by Merino *et al* to explain the different moiré superstructures of graphene on metals [45]. In their model, discrete rotation angles have been selected by a calculation with an accuracy of 0.05°, which is a great step forward relative to the continuous model. However, there are still some unsolved problems in this model, for example, the detailed structural configurations of the lattices of two stacked layers as well as the commensurability of the moiré superstructure. These items are very important to get real space information and the geometric matrices needed for theoretical simulations and understanding of the electronic properties. In the following, we extend an improved HOC method [55] to gain an approximate formula for the analysis

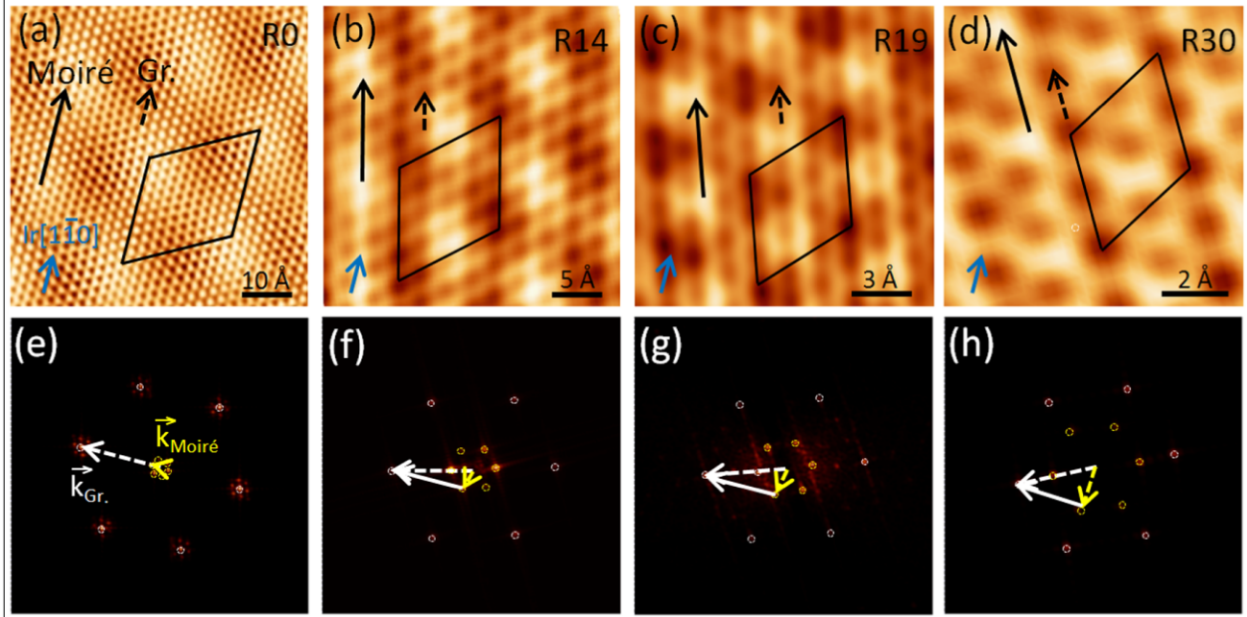


Figure 2. Atomic resolution STM images of R0, R14, R19, and R30 graphene on Ir(111) (a)–(d) and corresponding FFT patterns (e)–(f). Four black rhombuses in (a)–(d) indicate the corresponding unit cell of the four moiré superstructures. The blue arrows show the direction of Ir[110]; The solid and dashed arrows indicate the directions of the moiré superstructure and graphene [1120], respectively. (e)–(h) The reciprocal lattice vectors of graphene, moiré superstructure, and the Ir substrate are denoted by dashed white, yellow, and solid arrows, respectively. All FFT spots are highlighted by small dashed circles.

of the moiré superstructures, which is able to give a correct and detailed description of the configurations for all possible commensurate moiré superstructures of graphene on Ir(111).

Figure 3(a) shows a typical example of HOC structures. The black rhombus represents a $(\sqrt{3} \times \sqrt{3})R30^\circ$ superstructure of the adsorbed layer (red balls). At the same time, it represents a (4×4) superstructure of the substrate (gray balls). To embody both structures, it can be described as $(\sqrt{3} \times \sqrt{3})A/(4 \times 4)S$, and an equation can be deduced from this structure: $\sqrt{3}A = 4S$, where A and S are the lattice parameters of the adsorbed layer and the substrate, respectively. For further application with random specific lattices, the equation turns into the following format: $\sqrt{mA} = \sqrt{nS}$. Here, m and n are the so-called hexagonal numbers [46]. This model is assumed to be a rigid model. In a graphene–metal system, both the adsorbed layer and the substrate may be stretched or compressed a little to reach the most stable state. Thus, the above equation can be modified into an approximate formula: $\sqrt{mA} \approx \sqrt{nS}$. A systematic procedure for identifying the hexagonal number (m and n) has previously been proposed in terms of arithmetic [46], here we introduce a simple method to obtain these numbers in a hexagonal lattice from a geometric point of view.

Figure 3(b) illustrates a hexagonal lattice, in which the number represents the distance (d) from the origin point $(0, 0)$ to the corresponding lattice point in this hexagonal array. A lattice hexagonal number (m or n) can be obtained by the equation of $m = d^2$. Each number can be used for either graphene adlayer (m) or the underlying substrate (n). Now we can reveal all possible HOC structures by using the above approximate formula: $\sqrt{mA} \approx \sqrt{nS}$, where $A = 2.4612 \text{ \AA}$ for

graphene and $S = 2.7150 \text{ \AA}$ for Ir(111). Because the observed largest periodicity of the moiré superstructures is about 25 \AA , as the R0 graphene shown in figure 2(a), we get a list of 21 HOC structures and their corresponding structural parameters with the unit length smaller than 25 \AA , as shown in table 1. Note that, although we only calculate the HOC structures within the range of 0° – 30° , there is a counterpart in the range of 30° – 60° , which is also possible for the formation of HOC structures. In table 1, we provide some useful structural data, including the unit cell of moiré superstructures, the oriented angle of the graphene lattice relative to the substrate lattice, the nominal mismatch between two lattices, and even the matrix.

In these 21 HOC structures in table 1, we can find six moiré superstructures of graphene on Ir(111) we observed experimentally. The patterns of R0, R14, R19, R23, R26, and R30 described in figure 1 correspond to structures 20, 3, 2, 4, 7, and 1 in table 1, respectively. The oriented angle of each graphene moiré superstructure relative to the substrate obviously fits very well with the experimental data. Besides the orientation, the unit size is also in good agreement with the STM observations shown in figure 2. Moreover, the precise matrix can be obtained in this table, especially for graphene domains of R23 and R26, although we do not get the atomic resolution STM images of them.

Due to the mismatch, graphene either compresses or stretches a little on the substrate. Commonly, the less stress graphene endures, the higher the probability of moiré superstructures appearing. Nevertheless, from our results, it seems that the mismatch cannot be a reference for the priority of the emergence of moiré superstructures. For instance, R30

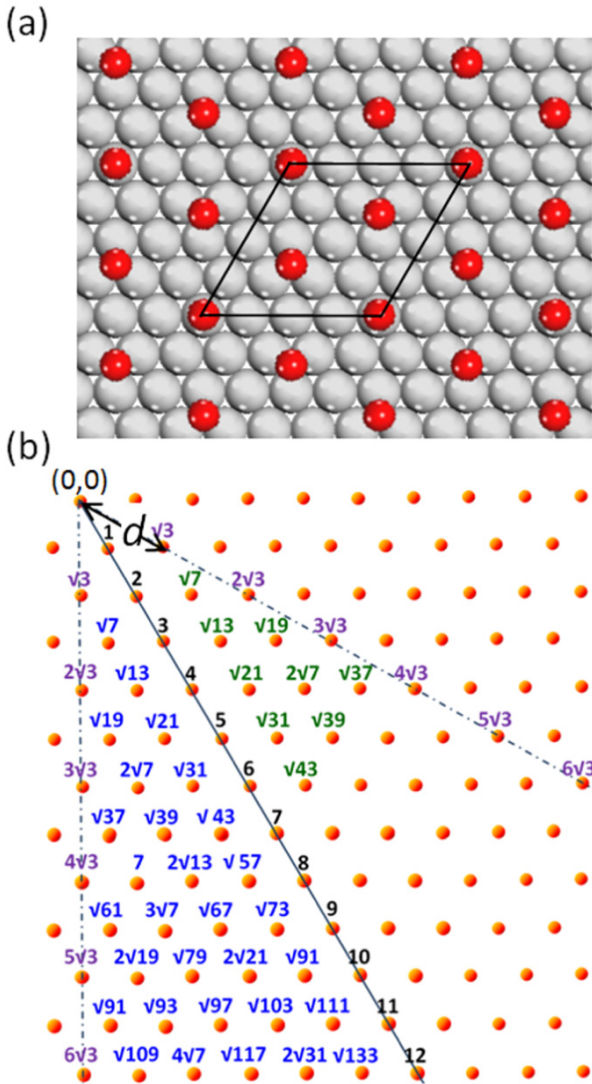


Figure 3. (a) An example of HOC structure: a $(\sqrt{3} \times \sqrt{3})R30^\circ$ superstructure is commensurate with a (4×4) lattice of the substrate. The gray and red balls illustrate the atoms of the substrate and the adsorbate layer, respectively. (b) A hexagonal lattice, in which the number represents the distance (d) from the origin point $(0, 0)$ to the corresponding lattice point in the array. The numbers in the range of 0° – 30° have counterparts in 30° – 60° .

graphene has a relative mismatch of -4.47% , which is much larger than most other moiré superstructures; however, the probability of its emergence is not lower than other rotations of graphene. Although we cannot predict the emergence of moiré superstructures based on the mismatch, as long as a moiré superstructure is characterized by LEED or STM, all the relative geometric information, including the matrix, the rotation angle between the graphene lattice and the substrate, the rotation angle between the graphene and the moiré superstructure, can be derived immediately by the approximate HOC formula. This suggests that the information in table 1 can serve as a database of moiré superstructures, which is very helpful for the analysis of experimental results and construction of theoretical models.

We also use this improved HOC method to check the reported moiré superstructures of graphene on Pt(111) [26], Pd(111) [56], Cu(111) [24], Ni(111) [57], all of which fit very well with the experimental data. In addition, we compared our results with those derived from the strain-driven model [45], all reported moiré superstructures can be found in our HOC structures. Furthermore, our data provide the precise matrices, which are essentially important for understanding the chemical and physical properties and the theoretical simulations. This method can also be applied to bilayer graphene, where the lattice constants of the two layers are the same ($A = S$).

3.3. Interface structures and electronic properties

In order to gain a deep understanding of multi-oriented moiré superstructures on Ir(111), we conducted theoretical calculations by using DFT + D/PBE methods. The relaxed structural models, the corresponding simulated STM images, and the electron transfer at the graphene–Ir interface are shown in figure 4. Table 2 summarizes the details of the optimized geometric parameters and the electron transfer at the graphene–Ir interface of all six moiré superstructures. In our models, the interface distance (h) between the lowest carbon atom and the first layer of the Ir substrate in all six structures is around 3.2 \AA , with the lowest value of 3.16 \AA in the R30 domain and the highest value of 3.32 \AA in the R26 domain, which is very close to the interlayer distance of graphite. Nevertheless, the interface distances of all six superstructures are small compared to that of a strongly bonded graphene–metal system, like graphene on Ru(0001) [16]. This may suggest a weak interaction at the graphene–Ir(111) interface regardless of the domain orientations. In order to verify this, we further calculated the electron transfer at the interface as discussed later.

As for the atomic arrangement of the relaxed moiré superstructures, R0 graphene (see figure 5(a)) has three special regions which depend on the location of a carbon hexagon relative to the underlying iridium atom in the substrate: on top of the first (named as top region), second (fcc region), or third (hcp region) layer atoms [17]. For the R14 and R19 graphene, due to their relatively small moiré unit cells compared to R0 graphene, it is a little difficult to figure out these three regions in the optimized moiré superstructures, as shown in figures 4(a) and (d).

The optimized atomic superstructures of R23 and R26 graphene are more complicated. First, the corresponding graphene lattices of the two moiré superstructures are derived by the HOC method, which is $(\sqrt{19} \times \sqrt{19})$ and $(\sqrt{37} \times \sqrt{37})$, respectively. Unlike the other four lattices, these values are not integral multiple of the lattice vector of graphene. The orientations of the moiré superstructures are not parallel to the graphene lattice, as confirmed by the models in figures 4(g) and (j). Second, for these two superstructures we find the top region where the carbon hexagonal-ring sits directly atop one iridium atom, but we find no concentrated fcc or hcp regions. This is probably the reason for the smaller corrugation. This

Table 1. All possible HOC superstructures of graphene on Ir(111). For the lattice parameters, we have chosen $A = 2.4612 \text{ \AA}$ for graphene and $S = 2.715 \text{ \AA}$ for Ir(111). Here, $\Delta = L_{\text{Ir}} - L_{\text{G}}$, and its value is less than 0.2 \AA for all HOC structures in the list except for the first one ($\Delta = 0.22 \text{ \AA}$). The symbol ‘-’ before the relative mismatch means graphene is compressed to form an HOC structure. All the angles are obtained by geometric calculations.

	HOC structures	$L_{\text{Ir}}/L_{\text{G}}$ (Å)	Relative mismatch Δ/L_{G} (%)	Angle of Gr to Ir(111) (deg)	Angle between moiré and Gr (deg)	Matrix
1	G(2 × 2)/Ir(√3 × √3)	4.92/4.70	-4.47	30	0	$G \begin{bmatrix} 2 & 0 \\ 0 & 2 \end{bmatrix} / \text{Ir} \begin{bmatrix} 2 & 1 \\ -1 & 1 \end{bmatrix}$
2	G(3 × 3)/Ir(√7 × √7)	7.38/7.18	-2.91	19.11	0	$G \begin{bmatrix} 3 & 0 \\ 0 & 3 \end{bmatrix} / \text{Ir} \begin{bmatrix} 3 & 1 \\ -1 & 2 \end{bmatrix}$
3	G(4 × 4)/Ir(√13 × √13)	9.84/9.79	-0.55	13.90	0	$G \begin{bmatrix} 4 & 0 \\ 0 & 4 \end{bmatrix} / \text{Ir} \begin{bmatrix} 4 & 1 \\ -1 & 3 \end{bmatrix}$
4	G(√19 × √19)/Ir(4 × 4)	10.73/10.86	1.23	23.41	23.41	$G \begin{bmatrix} 5 & 2 \\ -2 & 3 \end{bmatrix} / \text{Ir} \begin{bmatrix} 4 & 0 \\ 0 & 4 \end{bmatrix}$
5	G(5 × 5)/Ir(√21 × √21)	12.31/12.44	1.11	10.89	0	$G \begin{bmatrix} 5 & 0 \\ 0 & 5 \end{bmatrix} / \text{Ir} \begin{bmatrix} 5 & 1 \\ -1 & 4 \end{bmatrix}$
6	G(√31 × √31)/Ir(5 × 5)	13.70/13.58	-0.94	8.95	8.95	$G \begin{bmatrix} 6 & 1 \\ -1 & 5 \end{bmatrix} / \text{Ir} \begin{bmatrix} 5 & 0 \\ 0 & 5 \end{bmatrix}$
7	G(√37 × √37)/Ir(√31 × √31)	14.97/15.12	0.97	16.34/25.77	25.28	$G \begin{bmatrix} 7 & 3 \\ -3 & 4 \end{bmatrix} / \text{Ir} \begin{bmatrix} 6 & 1 \\ -1 & 5 \end{bmatrix}$
8	G(√43 × √43)/Ir(6 × 6)	16.14/16.29	0.94	7.59	7.59	$G \begin{bmatrix} 7 & 1 \\ -1 & 6 \end{bmatrix} / \text{Ir} \begin{bmatrix} 6 & 0 \\ 0 & 6 \end{bmatrix}$
9	G(2√13 × 2√13)/Ir(√43 × √43)	17.15/17.80	0.31	6.31/21.49	13.90	$G \begin{bmatrix} 8 & 2 \\ -2 & 6 \end{bmatrix} / \text{Ir} \begin{bmatrix} 7 & 1 \\ -1 & 6 \end{bmatrix}$
10	G(3√7 × 3√7)/Ir(2√13 × 2√13)	19.53/19.58	0.22	5.21/27.00	19.11	$G \begin{bmatrix} 9 & 3 \\ -3 & 6 \end{bmatrix} / \text{Ir} \begin{bmatrix} 8 & 2 \\ -2 & 6 \end{bmatrix}$
11	G(√73 × √73)/Ir(√61 × √61)	21.03/21.20	0.84	20.51/27.85	5.82	$G \begin{bmatrix} 9 & 1 \\ -1 & 8 \end{bmatrix} / \text{Ir} \begin{bmatrix} 9 & 4 \\ -4 & 5 \end{bmatrix}$
12	G(5√3 × 5√3)/Ir(√61 × √61)	21.31/21.20	-0.52	3.67	30	$G \begin{bmatrix} 10 & 5 \\ -5 & 5 \end{bmatrix} / \text{Ir} \begin{bmatrix} 9 & 4 \\ -4 & 5 \end{bmatrix}$
13	G(2√19 × 2√19)/Ir(3√7 × 3√7)	21.46/21.55	0.43	4.31/17.48	23.41	$G \begin{bmatrix} 10 & 4 \\ -4 & 6 \end{bmatrix} / \text{Ir} \begin{bmatrix} 9 & 3 \\ -3 & 6 \end{bmatrix}$
14	G(√79 × √79)/Ir(8 × 8)	21.88/21.72	0.71	17.00	17.00	$G \begin{bmatrix} 10 & 3 \\ -3 & 7 \end{bmatrix} / \text{Ir} \begin{bmatrix} 8 & 0 \\ 0 & 8 \end{bmatrix}$
15	G(9 × 9)/Ir(√67 × √67)	22.15/22.22	0.32	12.22	0	$G \begin{bmatrix} 9 & 0 \\ 0 & 9 \end{bmatrix} / \text{Ir} \begin{bmatrix} 9 & 2 \\ -2 & 7 \end{bmatrix}$
16	G(√91 × √91)/Ir(5√3 × 5√3)	23.48/23.51	0.15	3.00/24.79	5.21/27.00	$G \begin{bmatrix} 10 & 1 \\ -1 & 9 \end{bmatrix} / \text{Ir} \begin{bmatrix} 10 & 5 \\ -5 & 5 \end{bmatrix}$ $G \begin{bmatrix} 11 & 5 \\ -5 & 6 \end{bmatrix} / \text{Ir} \begin{bmatrix} 10 & 5 \\ -5 & 5 \end{bmatrix}$

may help explain why the simulated STM images of these two superstructures have no obvious moiré pattern.

For the R30 graphene, the corresponding graphene lattice is (2 × 2), just twice as large as the graphene honeycomb lattice and quite a bit smaller than that in the other superstructures,

thus the so-called fcc and hcp regions are almost the same, where one carbon atom locates atop one iridium atom, as shown in figure 4(m). Only two types of carbon atoms can be sorted out: those located directly atop one iridium atom (*A* atom) and those adjacent to *A* atoms (*B* atom). The simulated

Table 1. (Continued.)

HOC structures		$L_{\text{Ir}}/L_{\text{G}}$ (Å)	Relative mismatch Δ/L_{G} (%)	Angle of Gr to Ir(111) (deg)	Angle between moiré and Gr (deg)	Matrix
17	$G(\sqrt{91} \times \sqrt{91})/\text{Ir}(2\sqrt{19} \times 2\sqrt{19})$	23.48/23.67	0.82	3.58/9.59 18.20/28.62	5.21/27.00	$G \begin{bmatrix} 10 & 1 \\ -1 & 9 \end{bmatrix} / \text{Ir} \begin{bmatrix} 10 & 4 \\ -4 & 6 \end{bmatrix}$ $G \begin{bmatrix} 11 & 5 \\ -5 & 6 \end{bmatrix} / \text{Ir} \begin{bmatrix} 10 & 4 \\ -4 & 6 \end{bmatrix}$
18	$G(\sqrt{93} \times \sqrt{93})/\text{Ir}(2\sqrt{19} \times 2\sqrt{19})$	23.75/23.67	-0.32	2.36/15.54	21.05	$G \begin{bmatrix} 11 & 4 \\ -4 & 7 \end{bmatrix} / \text{Ir} \begin{bmatrix} 10 & 4 \\ -4 & 6 \end{bmatrix}$
19	$G(\sqrt{97} \times \sqrt{97})/\text{Ir}(\sqrt{79} \times \sqrt{79})$	24.24/24.13	-0.45	1.70/27.70	15.30	$G \begin{bmatrix} 11 & 3 \\ -3 & 8 \end{bmatrix} / \text{Ir} \begin{bmatrix} 10 & 3 \\ -3 & 7 \end{bmatrix}$
20	$G(10 \times 10)/\text{Ir}(9 \times 9)$	24.61/24.44	-0.72	0	0	$G \begin{bmatrix} 10 & 0 \\ 0 & 10 \end{bmatrix} / \text{Ir} \begin{bmatrix} 9 & 0 \\ 0 & 9 \end{bmatrix}$
21	$G(\sqrt{103} \times \sqrt{103})/\text{Ir}(2\sqrt{21} \times 2\sqrt{21})$	24.98/24.88	-0.38	1.07/20.72	9.83	$G \begin{bmatrix} 11 & 2 \\ -2 & 9 \end{bmatrix} / \text{Ir} \begin{bmatrix} 10 & 2 \\ -2 & 8 \end{bmatrix}$

Table 2. DFT + D/PBE calculated results of the geometric parameters and the electron transfer at the graphene–Ir interface of all the six rotated moiré superstructures. The corresponding graphene lattices are listed in the first row. ‘ h ’ denotes the distance between the lowest carbon atom and the first layer of Ir substrate. ‘ Δh ’ means the depth of corrugation of the graphene adlayer (distance between the highest carbon atom and the lowest carbon atom).

	R0	R14	R19	R23	R26	R30
Moiré lattice	$G(10 \times 10)$	$G(4 \times 4)$	$G(3 \times 3)$	$G(\sqrt{19} \times \sqrt{19})$	$G(\sqrt{37} \times \sqrt{37})$	$G(2 \times 2)$
$h(\text{Ir-C})$	3.159	3.22	3.289	3.27	3.317	3.29
$\Delta h(\text{C-C})$	0.423	0.101	0.051	0.022	0.015	0.014
Charge transfer (e/C)	0.012	0.014	0.013	0.011	0.012	0.014

STM image in figure 4(n) exhibits a clear contrast between *A* and *B*: the local density states of *B* carbon atoms are stronger than that of *A* carbon atoms, and hence the *B* carbon atoms look brighter.

We further investigated the electronic properties of all six rotated superstructures by calculating the charge distribution at the graphene–Ir(111) interface. Globally electrons transfer from the graphene layer to the Ir substrate, as shown in figures 4(c), (f), (i), (l), and (o). For example, figure 4(o) shows a cross-section of the electron density differences and the planar integration of electron density differences along the *c*-direction of R30 graphene. We find that electrons mainly redistribute between graphene and iridium substrate, and the graphene is slightly p doped where the electron loss is about 0.014 electrons per carbon atom (e/C, see table 2). R0 graphene calculated previously by Busse *et al* showed a similar feature of electron transfer [58]. From table 2, we can see that the electron transfer of all the six rotated graphenes are at the same order of magnitude (0.01–0.014 e/C), which is much smaller than that of the Gr/Ru(0001) system [15]. It demonstrates that the relatively weak interaction exists globally at the graphene–Ir interface in all different rotated

domains. This would be the main reason for the coexistence of different moiré superstructures.

We also found that different regions with different geometric corrugation (atom arrangements) in the superstructure have different local electric properties. For example, the corrugation of R0 graphene is larger than that of other rotated graphenes (see table 2, Δh). It has three different regions described as top, fcc, and hcp sites (figure 5(a)). The simulated STM image clearly shows the same moiré superstructure as the experimental observations (figure 5(b)). We calculated the electron transfer of each *A* and *B* atom in these regions. To calculate the electron transfer, we drew a column with radius of 0.7 Å (half a C–C bond length) by setting *A/B* atoms as the center point, then integrated the electron density difference. It turns out that the electron loss of carbon atoms in the top site is the least, while that of *A* and *B* atoms in fcc (or hcp) regions is 0.008 and 0.003 e/C larger, respectively. This means that the carbon atoms in the fcc/hcp sites have stronger hybridization with the underlying Ir atoms than that in top sites in R0 graphene [58]. Previous experimental data using Raman spectroscopy [59] demonstrate that no Raman signal was detected in R0 graphene, in contrast, the

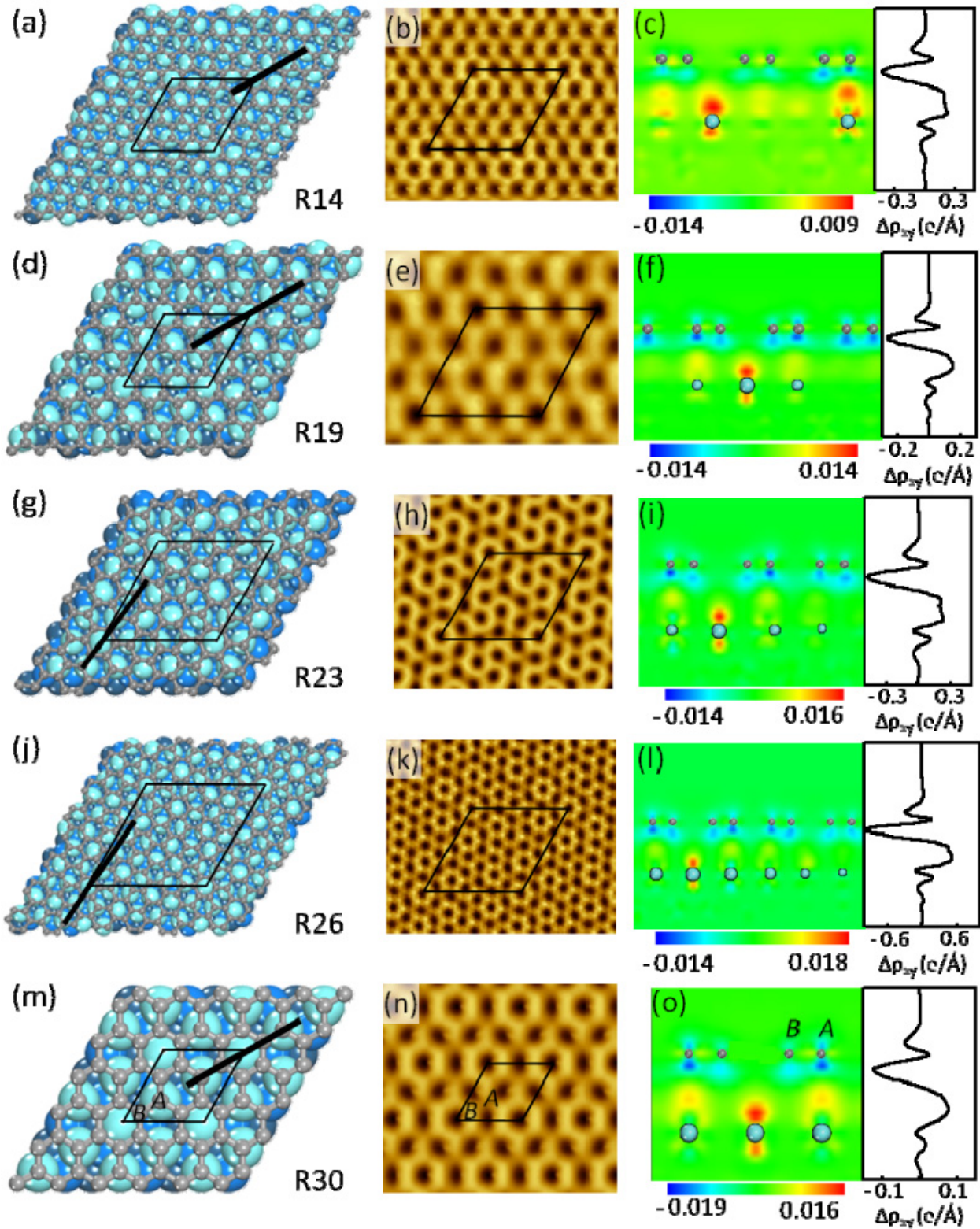


Figure 4. Top view of the optimized superstructures ((a), (d), (g), (j), and (m)), the corresponding simulated STM images ((b), (e), (h), (k), and (n)) and the cross-section (along the thick black line in (a), (d), (g), (j), and (m)) of the electron density differences calculated by DFT + D/PBE methods ((c), (f), (i), (l), and (o)) of R14, R19, R23, R26, and R30 graphene, respectively. The black rhombuses indicate the respective unit cells of the moiré superstructures. The letter A depicts the carbon atom located atop of an iridium atom, and B depicts the adjacent carbon atom of A.

vibrational modes were detected in the R30 graphene. From our calculation results, globally the electron transfers of R0 and R30 graphene are close to each other, both exhibiting

a relatively weak hybridization of carbon atoms with the underlying Ir atoms. But in R0 graphene the hybridization mainly localizes in the hcp/fcc sites, which probably causes

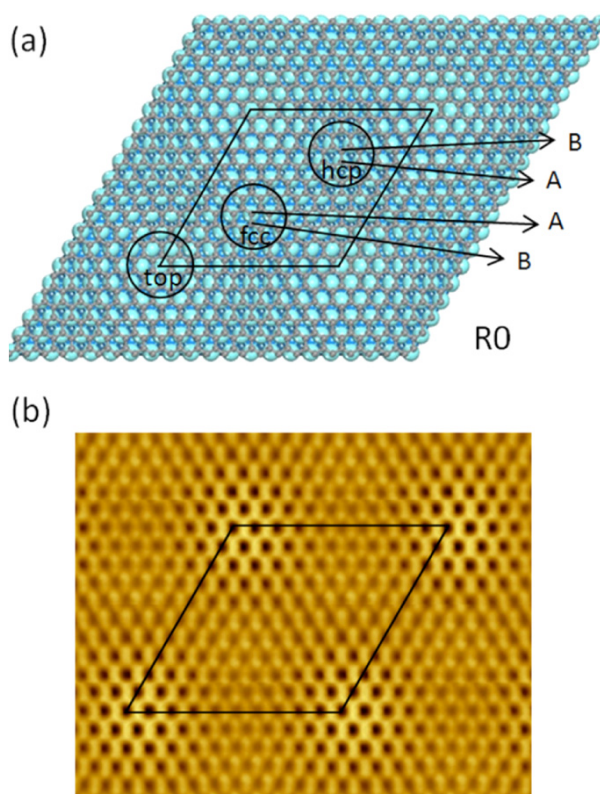


Figure 5. Top view of the relaxed moiré superstructure (a) and the simulated STM image of R0 graphene calculated by DFT + D/PBE methods (b). The black rhombus indicates a unit cell of the moiré pattern. The A and B carbon atoms in the hcp/fcc regions are indicated by black arrows.

the differences of the Raman signal of R0 graphene to R30 graphene.

4. Conclusions

In summary, we report on six different rotated moiré superstructures of graphene on Ir(111) characterized by experimental observations of LEED, STM, and DFT calculations, named R0, R14, R19, R23, R26, and R30 graphene. The moiré pattern of R0 graphene has remarkable diffraction spots and the largest corrugation of the six rotated graphene domains. The overall relative orientation of the graphene lattice and the moiré superstructures of R0, R14, R19, and R30 graphene were parallel in every case, but R23 and R26 graphene are not so aligned. We further use the improved HOC method, which is demonstrated to be very useful to get a better understanding of the configuration and helpful for the analysis of experimental data and the construction of models for theoretical calculations, to produce a whole list of possible superstructures of graphene on Ir(111). By using DFT+D/PBE calculations on the six superstructures we observed, we further revealed the detailed geometric environment and interface electronic structures of graphene on the Ir(111) system. The electron transfer at the interface of the graphene–Ir substrate demonstrates the relatively weak interactions in all the six rotated moiré superstructures.

Acknowledgments

This work was financially supported by MOST (Nos 2011CB932700, 2011CB921702, and 2011CB828401), NNSFC, CAS, and SSC in China.

References

- [1] Novoselov K S, Geim A K, Morozov S V, Jiang D, Zhang Y, Dubonos S V, Grigorieva I V and Firsov A A 2004 *Science* **306** 666
- [2] Zhang Y B, Tan Y W, Stormer H L and Kim P 2005 *Nature* **438** 201
- [3] Geim A K and Novoselov K S 2007 *Nature Mater.* **6** 183
- [4] Tombros N, Jozsa C, Popinciuc M, Jonkman H T and van Wees B J 2007 *Nature* **448** 571
- [5] Novoselov K S *et al* 2007 *Science* **315** 1379
- [6] Wang F, Zhang Y B, Tian C S, Girit C, Zettl A, Crommie M and Shen Y R 2008 *Science* **320** 206
- [7] Berger C *et al* 2006 *Science* **312** 1191
- [8] Stankovich S, Dikin D A, Dommett G H B, Kohlhaas K M, Zimney E J, Stach E A, Piner R D, Nguyen S T and Ruoff R S 2006 *Nature* **442** 282
- [9] Pan Y, Shi D X and Gao H J 2007 *Chin. Phys.* **16** 3151
- [10] Kim K S *et al* 2009 *Nature* **457** 706
- [11] Dedkov Y S, Fonin M, Rudiger U and Laubschat C 2008 *Phys. Rev. Lett.* **100** 107602
- [12] Wu M C, Xu Q and Goodman D W 1994 *J. Phys. Chem.* **98** 5104
- [13] de Parga A L V, Calleja F, Borca B, Passeggi M C G, Hinarejos J J, Guinea F and Miranda R 2008 *Phys. Rev. Lett.* **100** 056807
- [14] Sutter P W, Flege J I and Sutter E A 2008 *Nature Mater.* **7** 406
- [15] Wang B, Bocquet M L, Marchini S, Gunther S and Wintterlin J 2008 *Phys. Chem. Chem. Phys.* **10** 3530
- [16] Pan Y, Zhang H G, Shi D X, Sun J T, Du S X, Liu F and Gao H J 2009 *Adv. Mater.* **21** 2777
- [17] N'Diaye A, Bleikamp S, Feibelman P and Michely T 2006 *Phys. Rev. Lett.* **97** 215501
- [18] Coraux J, N'Diaye A T, Busse C and Michely T 2008 *Nano Lett.* **8** 565
- [19] N'Diaye A T, Coraux J, Plasa T N, Busse C and Michely T 2008 *New J. Phys.* **10** 043033
- [20] Feibelman P 2008 *Phys. Rev. B* **77** 165419
- [21] N'Diaye A T, Engler M, Busse C, Wall D, Buckanie N, Meyer zu Heringdorf F-J, van Gastel R, Poelsema B and Michely T 2009 *New J. Phys.* **11** 023006
- [22] Feibelman P 2009 *Phys. Rev. B* **80** 085412
- [23] Li X S *et al* 2009 *Science* **324** 1312
- [24] Gao L, Guest J R and Guisinger N P 2010 *Nano Lett.* **10** 3512
- [25] Sutter P, Sadowski J T and Sutter E 2009 *Phys. Rev. B* **80** 245411
- [26] Gao M, Pan Y, Huang L, Hu H, Zhang L Z, Guo H M, Du S X and Gao H J 2011 *Appl. Phys. Lett.* **98** 033101
- [27] Loginova E, Nie S, Thurmer K, Bartelt N C and McCarty K F 2009 *Phys. Rev. B* **80** 085430
- [28] Nie S, Walter A L, Bartelt N C, Starodub E, Bostwick A, Rotenberg E and McCarty K F 2011 *ACS Nano* **5** 2298
- [29] Hattab H *et al* 2011 *Appl. Phys. Lett.* **98** 141903
- [30] Pan Y, Gao M, Huang L, Liu F and Gao H J 2009 *Appl. Phys. Lett.* **95** 093106
- [31] Mao J H, Zhang H G, Jiang Y H, Pan Y, Gao M, Xiao W D and Gao H J 2009 *J. Am. Chem. Soc.* **131** 14136
- [32] Balog R *et al* 2010 *Nature Mater.* **9** 315
- [33] Luican A, Li G H, Reina A, Kong J, Nair R R, Novoselov K S, Geim A K and Andrei E Y 2011 *Phys. Rev. Lett.* **106** 126802

- [34] Miller D L, Kubista K D, Rutter G M, Ruan M, de Heer W A, First P N and Strosio J A 2009 *Science* **324** 924
- [35] Borca B *et al* 2010 *Phys. Rev. Lett.* **105** 036804
- [36] Zhang H G, Hu H, Pan Y, Mao J H, Gao M, Guo H M, Du S X, Greber T and Gao H J 2010 *J. Phys.: Condens. Matter* **22** 302001
- [37] Feng W, Lei S L, Li Q X and Zhao A D 2011 *J. Phys. Chem. C* **115** 24858
- [38] Armbrust N, Gudde J, Jakob P and Hofer U 2012 *Phys. Rev. Lett.* **108** 056801
- [39] Zhang H G and Greber T 2010 *Phys. Rev. Lett.* **105** 219701
- [40] Novaco A D and Mctague J P 1977 *Phys. Rev. Lett.* **38** 1286
- [41] Mctague J P and Novaco A D 1979 *Phys. Rev. B* **19** 5299
- [42] Fuselier C R, Raich J C and Gillis N S 1980 *Surf. Sci.* **92** 667
- [43] Doering D L 1985 *J. Vac. Sci. Technol. A* **3** 809
- [44] Grey F and Bohr J 1992 *Europhys. Lett.* **18** 717
- [45] Merino P, Svec M, Pinardi A L, Otero G and Martin-Gago J A 2011 *ACS Nano* **5** 5627
- [46] Tkatchenko A 2007 *Phys. Rev. B* **75** 235411
- [47] Vanderbilt D 1990 *Phys. Rev. B* **41** 7892
- [48] Kresse G and Furthmuller J 1996 *Phys. Rev. B* **54** 11169
- [49] Perdew J P, Burke K and Ernzerhof M 1996 *Phys. Rev. Lett.* **77** 3865
- [50] Grimme S 2006 *J. Comput. Chem.* **27** 1787
- [51] Bucko T, Hafner J, Lebegue S and Angyan J G 2010 *J. Phys. Chem. A* **114** 11814
- [52] Tonigold K and Gross A 2010 *J. Chem. Phys.* **132** 224701
- [53] Cervenka J and Flipse C F J 2007 *J. Phys. Conf. Ser.* **61** 190
- [54] Cervenka J and Flipse C F J 2009 *Phys. Rev. B* **79** 195429
- [55] Bak P 1982 *Rep. Progr. Phys.* **45** 587
- [56] Murata Y, Starodub E, Kappes B B, Ciobanu C V, Bartelt N C, McCarty K F and Kodambaka S 2010 *Appl. Phys. Lett.* **97** 143114
- [57] Murata Y, Petrova V, Kappes B B, Ebnonnasir A, Petrov I, Xie Y H, Ciobanu C V and Kodambaka S 2010 *ACS Nano* **4** 6509
- [58] Busse C *et al* 2011 *Phys. Rev. Lett.* **107** 036101
- [59] Starodub E, Bostwick A, Moreschini L, Nie S, Gabaly F, McCarty K and Rotenberg E 2011 *Phys. Rev. B* **83** 125428